Materials Horizons

ROYAL SOCIETY OF CHEMISTRY

COMMUNICATION

View Article Online
View Journal

Cite this: DOI: 10.1039/d6mh00065g

Received 13th January 2026,
Accepted 9th April 2026

DOI: 10.1039/d6mh00065g

rsc.li/materials-horizons

Rapid ambient direct growth of HKUST-1 *via* atmospheric pressure plasma treatment

Moriyuki Kanno, *[ab] Tsuyohito Ito, [b] Itaru Honma [a] and Kazuo Terashima *[b]

The integration of metal–organic framework (MOF) thin films into functional devices is currently hindered by high temperatures, prolonged processing times, and complex additives required by conventional fabrication methods. We demonstrated a plasma-assisted strategy to directly synthesize crystalline MOF films on metal substrates under ambient conditions and overcome these kinetic and processing limitations. We used a HKUST-1 on a copper substrate as a model system and demonstrated that continuous crystalline films are formed within minutes in an ethylene glycol solution without the need for thermal annealing or external metal precursors. The mechanistic investigation revealed that the plasma–liquid–solid interface functions as a unique reaction field providing a dual driving force. The plasma treatment induced a reaction by functioning as an electrochemical driver for anodic metal dissolution while simultaneously assisting in ligand deprotonation through the generation of reactive species such as hydroxyl and superoxide ions. This process is governed by a kinetic balance, where a specific processing window defined by the metal electrode potential and the ligand acidity distinguishes copper from other metals. These results indicate that atmospheric pressure plasma serves as a potent tool for interfacial coordination chemistry, provided that the electrochemical ion supply and acid–base kinetics are synchronized. This work establishes a design principle for the rapid and additive-free fabrication of MOF films, thus offering a foundation for the streamlined integration of functional porous layers into next-generation devices.

New concepts

This study introduces a novel conceptual framework for the growth of metal–organic framework (MOF) films by utilizing atmospheric pressure plasma as a driver at the plasma–liquid–solid interface. Unlike conventional methods that often depend on thermal budgets or conductive electrolytes containing chemical additives, plasma-induced interfacial reactions are demonstrated to induce rapid, additive-free crystallization directly on metal substrates. The central conceptual advance lies in defining the specific kinetic processing window that governs this non-equilibrium process. Decoupling the thermal and electrochemical driving forces reveals that interfacial film growth is dictated by the interplay between the metal's standard electrode potential and the ligand's acidity. Reaction outcomes are found to diverge based on the stability of surface passivation and the rate of metal dissolution, highlighting that the kinetic synchronization between anodic ion release and ligand deprotonation is a fundamental prerequisite for crystallization. This work advances the mechanistic understanding of plasma-assisted coordination chemistry, positioning the plasma–liquid–solid interface as a versatile reaction field for materials integration.

1. Introduction

Metal–organic frameworks (MOFs) are a class of crystalline porous materials constructed from metal ions or clusters coordinated to organic ligands. Their exceptional characteristics, including high surface areas, tunable pore structures, and chemical versatility, have made them highly attractive for a wide range of applications, such as gas storage and separation, catalysis, sensing, and drug delivery.[1–5] As MOF research has matured, the focus has shifted from bulk powders to thin films and membranes, which are crucial for integrating these materials into functional devices. MOF films offer unique advantages, including oriented growth, direct contact with functional interfaces, enhanced compatibility with micro-and nanoscale platforms, and promising advancements in selective separation, microelectronics, and membrane reactors.[6–9]

Despite their potential, the development of effective strategies for synthesizing MOF films remains a significant technical barrier. Conventional methods, such as solvothermal synthesis,[10,11] layer-by-layer assembly,[12–15] and secondary growth,[16,17] often require elevated temperatures, long reaction times, or the use of chemical additives such as bases or modulators. These requirements can hinder scalability, restrict compatibility with thermally sensitive substrates, and impose an environmental

[a] Institute of Multidisciplinary Research for Advanced Materials, Tohoku University, 2-1-1 Katahira, Aoba-ku, Sendai, Miyagi, 980-8577, Japan. E-mail: moriyuki.kanno.e4@tohoku.ac.jp
[b] Department of Advanced Materials Science, Graduate School of Frontier Sciences, The University of Tokyo, 5-1-5 Kashiwanoha, Kashiwa, Chiba, 277-8561, Japan. E-mail: kazuo@plasma.k.u-tokyo.ac.jp

burden owing to the disposal of chemical waste. Consequently, developing a rapid and additive-free synthetic pathway is essential for overcoming these kinetic and processing limitations, particularly for investigating alternative driving forces for interfacial MOF growth.

We explored a novel synthetic approach utilizing plasma technology to address these limitations. Plasma provides a non-equilibrium environment containing highly energetic species, such as electrons, ions, and radicals, offering a unique capability to promote surface reactions and accelerate chemical kinetics. Although plasma has been applied to modify MOF surfaces[18–22] and assist in powder synthesis,[23–28] its potential for the direct growth of MOF films, particularly through reactions at the solid–liquid interface, remains unexplored. Notably, conventional electrochemical methods for MOF film growth typically require the addition of supporting electrolytes to ensure conductivity and external metal precursors to supply ions.[29,30] In contrast, the plasma–liquid interface creates a unique reaction environment that bypasses these requirements, though the fundamental mechanisms governing its influence on coordination chemistry are not yet fully elucidated.

This study demonstrated a plasma-assisted strategy for the direct synthesis of MOF on metal substrates. As a proof-of-concept, HKUST-1, a representative copper-based framework, was fabricated directly on copper substrates. This approach enables the rapid formation of a crystalline MOF layer where the substrate itself serves as the exclusive metal source, eliminating the need for external metal precursors or supporting electrolytes. This study further investigated the underlying mechanism by comparing the reaction behaviors across different metal substrates and ligand types. The critical role of plasma as a dual driver for anodic metal dissolution and ligand deprotonation is elucidated, highlighting that interfacial film growth is governed by the kinetic alignment between the electrochemical ion supply and the acid–base chemistry at the interface.

2. Results and discussion

2.1. Rapid growth and characterization of HKUST-1 films

The plasma-assisted synthesis strategy is illustrated in Fig. 1. A precursor solution containing 1,3,5-benzenetricarboxylic acid (H_3BTC) dissolved in ethylene glycol (EG) was directly dispensed onto a rotating copper substrate under atmospheric pressure plasma irradiation. The structural and morphological evolution was examined as a function of the number of 10-μL-precursor droplets to investigate the film growth process. The formation of the crystalline HKUST-1 phase was confirmed using X-ray diffraction (XRD), Fourier Transform Infrared (FTIR) spectroscopy, and scanning electron microscopy (SEM).

As shown in Fig. 2(a), the XRD pattern of the synthesized film exhibits a distinct diffraction peak at a 2θ value of approximately 11.6°, which corresponds to the (222) planes of the crystalline HKUST-1 structure. Notably, for the sample prepared with 60 drops, an additional minor peak began to emerge at 17.5°, assigned to the (333) reflection. The progressive increase in the primary peak, along with the appearance of this higher-order reflection with an increasing number of solution drops and treatment time, demonstrated that the MOF film growth is cumulative and that crystallinity improves with repeated plasma treatments. The dominance of these (*hhh*) reflections, while other characteristic peaks such as (200) and (220) are nearly absent, suggests a potential preferred orientation along the [111] direction on the copper substrate. This orientation may be energetically favorable because the (111) facets of the face-centered cubic HKUST-1 structure are reported to possess the lowest surface energy among the primary crystallographic planes.[31] Alternatively, this could be attributed to the limited scattering volume of the thin MOF layer, where only the most intense reflections are discernible above the background signal of the metallic support.

The FTIR spectrum exhibited characteristic absorption bands, confirming the coordination of the organic linkers to the metal centers. Specifically, the prominent peak observed at 1649 cm^{-1} was attributed to the asymmetric stretching vibrations of the carboxylate groups (ν_{as}(COO)), whereas the band at 1377 cm^{-1} corresponded to the symmetric stretching modes (ν_{sym}(COO)).[32,33] In contrast to free H_3BTC, for which a strong C═O stretching band appears around 1700 cm^{-1}, this band is absent in the films, indicating complete deprotonation and coordination of the carboxylate groups to Cu centers as COO^- ligands. The separation between ν_{as} and ν_{sym} falls in the range typically reported for bridging bidentate carboxylates in Cu(II) paddle-wheel units, rather than for monodentate or chelating

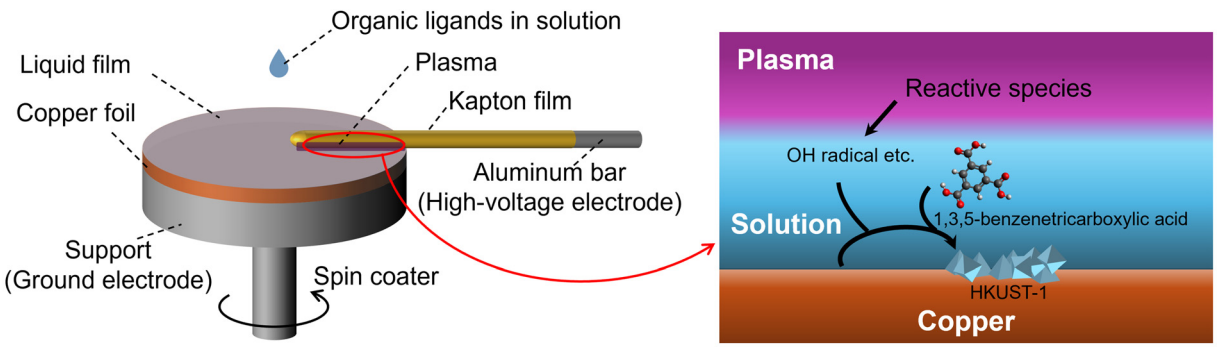

Fig. 1 Schematic illustration of the atmospheric-pressure plasma-assisted synthesis strategy for the rapid interfacial.

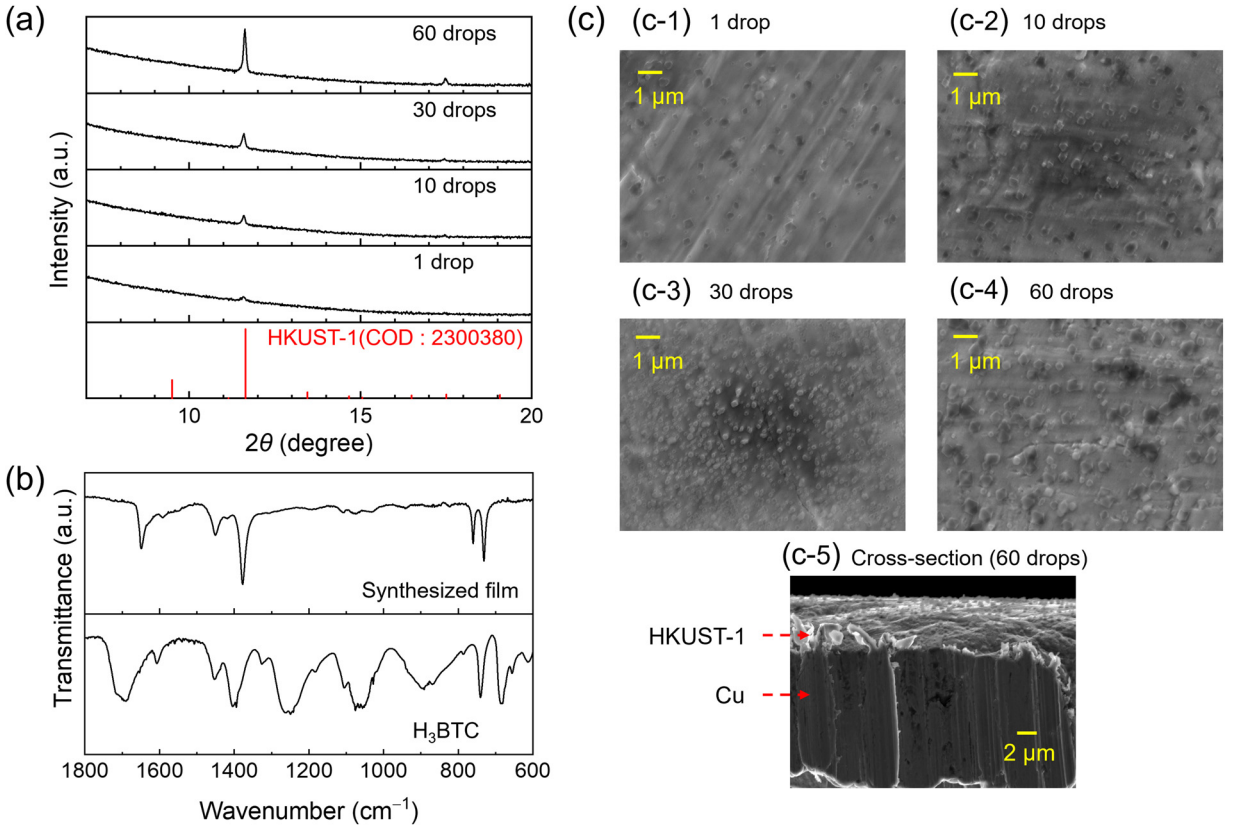

Fig. 2 Structural and morphological characterization of HKUST-1 films synthesized on copper substrates. (a) XRD patterns of films prepared with varying numbers of precursor drops (1, 10, 30, and 60 drops). The simulated pattern of HKUST-1 is shown at the bottom for reference. (b) FTIR spectra comparing the pristine H_3BTC ligand (bottom) and the plasma-synthesized film on copper substrate (top). (c) SEM images showing the morphological evolution of films: (c-1)–(c-4) Top-view images corresponding to 1, 10, 30, and 60 drops, respectively; (c-5) Cross-sectional view of the film formed with 60 drops.

modes,[32,33] thereby supporting the formation of μ_2-carboxylate-bridged Cu(II) dimers, which constitute the paddle-wheel secondary building units of the framework.

Additionally, the peak located at 1450 cm^{-1} was assigned to the C=C vibrations of the aromatic benzene ring.[34] The bands at 760 and 731 cm^{-1} in the lower wavenumber region were indicative of the Cu–O stretching vibrations[34] and the out-of-plane C–H bending of the aromatic ligands,[35] respectively. These observations collectively corroborate the formation of an HKUST-1-type Cu(II)-BTC framework constructed from Cu(II) paddle-wheel units on the Cu substrate.

SEM images revealed the morphological evolution of the HKUST-1 film. Top-view observations (Fig. 2(c)) indicate that the substrate surface was covered with interconnected crystals, exhibiting the characteristic polyhedral morphology of HKUST-1. As shown in Fig. 2(c-1)–(c-4), the surface coverage increased as the treatment proceeded, forming a continuous layer. These repeated cycles of solution delivery and plasma activation facilitate high-density nucleation and fill the gaps between existing crystals, ensuring the observed continuity and integration of the framework. While this interconnected network effectively covers the copper surface, the film thickness inherently exhibits a spatial distribution across the substrate. This variation is attributed to the dynamic nature of the solution dispensing process on a rotating substrate, influenced by centrifugal forces and the delivery cycles. Notably, the centrifugal force ensures that the precursor solution is spread into a thin liquid film, which prevents the localized piling up of materials directly under the stationary plasma. Furthermore, the cross-sectional view (Fig. 2(c-5)) confirmed that the HKUST-1 crystals grew directly from the copper surface, supporting the rapid plasma-induced interfacial growth. Although the current manual setup serves as a proof-of-concept, further enhancement of macroscopic uniformity is expected through the optimization of delivery systems, such as automated aerosol-assisted or spray-coating methods, to meet the requirements for large-scale device integration.

2.2. Role of plasma: electrochemical oxidation

Mechanistic insights into the metal ion supply were obtained by comparing plasma treatment with a conventional thermal process. Thermal control experiments, in which the copper substrate was heated with the precursor solution in an autoclave, demonstrated no detectable MOF growth by XRD (Fig. S2). However, FTIR spectroscopy revealed minor absorption bands associated with carboxylate coordination, suggesting limited surface interactions or formation of trace amorphous complexes. This discrepancy between the XRD and FTIR results indicates that although some short-range interfacial coordination occurs under

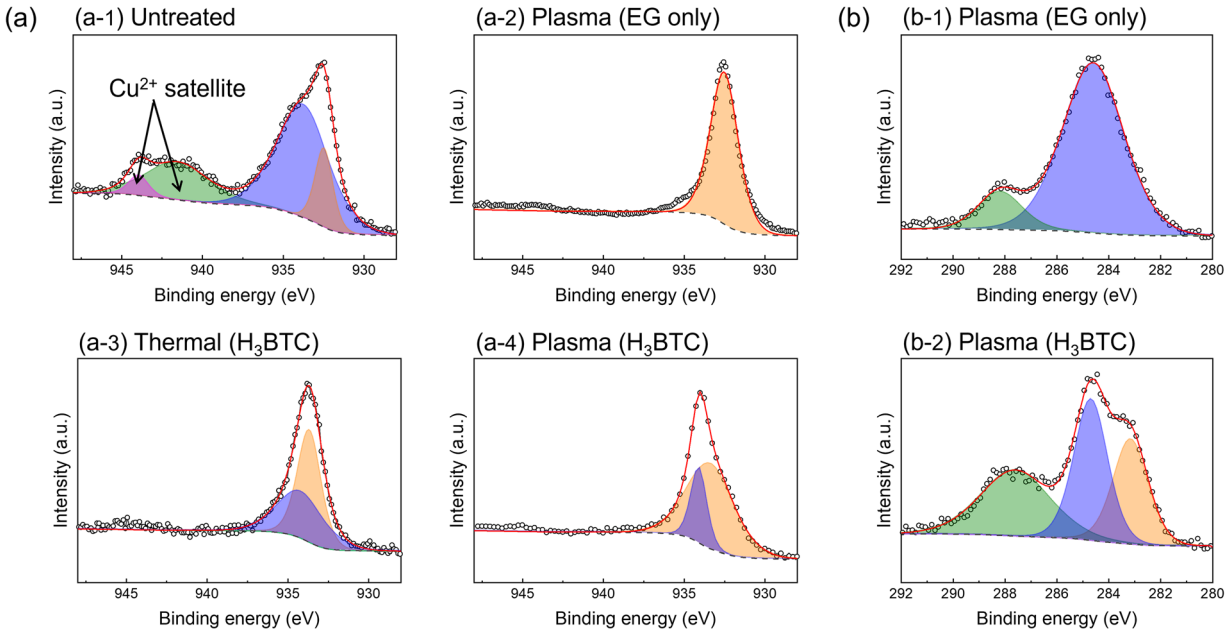

Fig. 3 Surface chemical analysis revealing the reaction mechanism. (a) Cu 2p XPS spectra of (a-1) untreated Cu foil, (a-2) foil treated with EG plasma, (a-3) foil treated solvothermally with H_3BTC/EG, and (a-4) foil treated with H_3BTC/EG plasma. (b) C 1s XPS spectra comparing (b-1) foil treated with EG plasma and (b-2) foil treated with H_3BTC/EG plasma.

thermal conditions, it is insufficient to initiate the nucleation and growth of a continuous crystalline lattice.

The surface chemical states were analyzed by X-ray photoelectron spectroscopy (XPS), as shown in Fig. 3(a), to investigate the origin of this behavior. The Cu 2p spectrum of the untreated copper substrate exhibited characteristic satellite peaks, indicating the presence of a native oxide layer (CuO).[36] Although previous studies have reported that Cu(II) species, such as hydroxides, can serve as reactive precursors for the rapid synthesis of HKUST-1,[37–42] these satellite peaks were absent in both thermally treated and plasma-treated samples. This spectral change suggests that the reducing atmosphere provided by EG effectively reduced the surface CuO to Cu(I) oxide (Cu_2O) or metallic species,[43] thereby eliminating the reactive oxide layer necessary for conventional acid–base reactions. Moreover, Cu(II) satellite peaks were absent in the HKUST-1 film spectrum synthesized by plasma treatment (Fig. 3(a-4)), despite the presence of Cu(II) paddlewheel units. This phenomenon was attributed to the partial surface reduction of Cu(II) to Cu(I) induced by X-ray irradiation during the XPS measurements as well as the reducing plasma environment.[26]

Based on these findings, we propose that the plasma treatment plays a critical role in establishing an electrochemical circuit with a grounded metal substrate. Under the applied AC voltage, the copper substrate periodically functions as an anode, thereby driving the electrochemical dissolution of copper ($Cu \rightarrow Cu^{2+} + 2e^-$) directly from the metallic surface into the solution. This plasma-induced anodic dissolution provides a continuous supply of Cu(II) ions necessary for crystal growth, a process in which thermal energy alone is insufficient to initiate once the reactive surface oxide is reduced.

Further evidence of the unique reaction environment at the plasma–liquid interface was provided by comparing the C 1s spectra of the ligand-free EG plasma treatment (Fig. 3(b-1)) and the HKUST-1-forming H_3BTC plasma process (Fig. 3(b-2)). The spectrum of the ligand-free sample is dominated by the C–C/C=C peak at 284.5 eV,[44] accompanied by a component around 288 eV attributable to oxidized carbon species generated during the plasma treatment. In contrast, the H_3BTC plasma-treated sample exhibits distinct features, which corroborate the growth of the HKUST-1 film. A prominent peak at approximately 288 eV was observed, corresponding to the carboxylate carbon (O–C=O) of the BTC ligand.[45] Crucially, a unique peak at a lower binding energy of 283 eV was exclusively detected in the HKUST-1 sample. This shift toward a lower binding energy is characteristic of carbon atoms bonding with metal species,[46,47] suggesting the formation of copper–carbon (Cu–C) bonds, possibly originating from the plasma-induced partial decomposition of organic precursors at the active interface. The formation of such specific interfacial species suggests that plasma treatment induces strong chemical interactions between the organic layer and the metal surface, which may serve as an anchoring layer to enhance the stability and adhesion of the HKUST-1 film.

2.3. Substrate dependency and kinetic balance

Although plasma serves as an oxidative driver for ion supply, the formation of crystalline films is not guaranteed for all metals. The method was applied to aluminum, nickel, and zinc substrates using the H_3BTC ligand to evaluate its generality. Control solvothermal experiments using metal nitrates confirmed that these metals were chemically capable of coordinating with H_3BTC to form solid complexes (Fig. S3). First, the

reaction behaviors of aluminum and nickel substrates were examined. In these cases, XRD and FTIR analyses revealed negligible reaction products (Fig. 4(a) and (b)). The lack of reactivity was confirmed by XPS analysis (Fig. 4(c-1) and (c-2)). The spectra indicated the persistent presence of stable passivation layers (native oxides, Al_2O_3, and NiO) even after plasma treatment. Although the metallic forms of aluminum and nickel possess standard electrode potentials that favor oxidation (−1.66 V and −0.26 V, respectively), their native oxide layers exhibit high chemical inertness against the acidic H_3BTC solution. This robust passivation layer effectively inhibited the initial metal dissolution process and prevented the supply of metal ions required for the reaction.

In contrast to the stable passivation layers observed for aluminum and nickel, zinc substrates exhibited reactivity. Although XRD analysis revealed no diffraction peaks indicating crystalline order (Fig. 4(a)), FTIR measurements detected weak absorption bands characteristic of metal–ligand coordination (Fig. 4(b)). Further evidence of the surface reaction was provided by the Zn 2p XPS spectrum (Fig. 4(c-3)), which displayed a discernible broadening toward higher binding energies compared to the untreated substrate. This indicated the chemical conversion of the surface species. Unlike inert oxides on aluminum and nickel, the native zinc oxide (ZnO) layer was chemically unstable in acidic precursor solutions and was susceptible to etching by carboxylate ligands. Consequently, the protective barrier was compromised, exposing the underlying metallic Zn. Considering that zinc possesses a lower standard electrode potential (−0.76 V) compared to copper (+0.34 V), it is proposed that the plasma induces an excessive electrochemical driving force. This possibly results in a rapid and uncontrolled release of ions that overwhelms the crystallization kinetics, leading to the formation of amorphous coordination complexes rather than a well-ordered lattice.

Consequently, the formation of crystalline HKUST-1 on copper is attributed to the unique kinetic balance between the effective removal of the protective passivation layer and the subsequent metal dissolution rate. Native oxides on copper are easily reduced or dissolved in the reaction environment, thereby exposing the active metal surface. The moderate reactivity of copper activated solely by the plasma environment provided an optimal ion release rate that was synchronized with the crystallization kinetics of the H_3BTC ligand. This balance is a critical factor that enables the oriented and continuous growth of the MOF film at the solid–liquid interface.

2.4. Ligand specificity and acid–base chemistry

To explore the versatility of the plasma-assisted process beyond carboxylate ligands, this investigation was extended to nitrogen-donor ligands. Specifically, 2-methylimidazole (2-MIM, pK_a ~14.4)[48] was selected as a model ligand. This compound is the standard precursor for Zeolitic Imidazolate Framework-8 (ZIF-8), a subclass of MOFs composed of zinc ions coordinated by 2-MIM linkers, and is widely recognized for its high porosity and

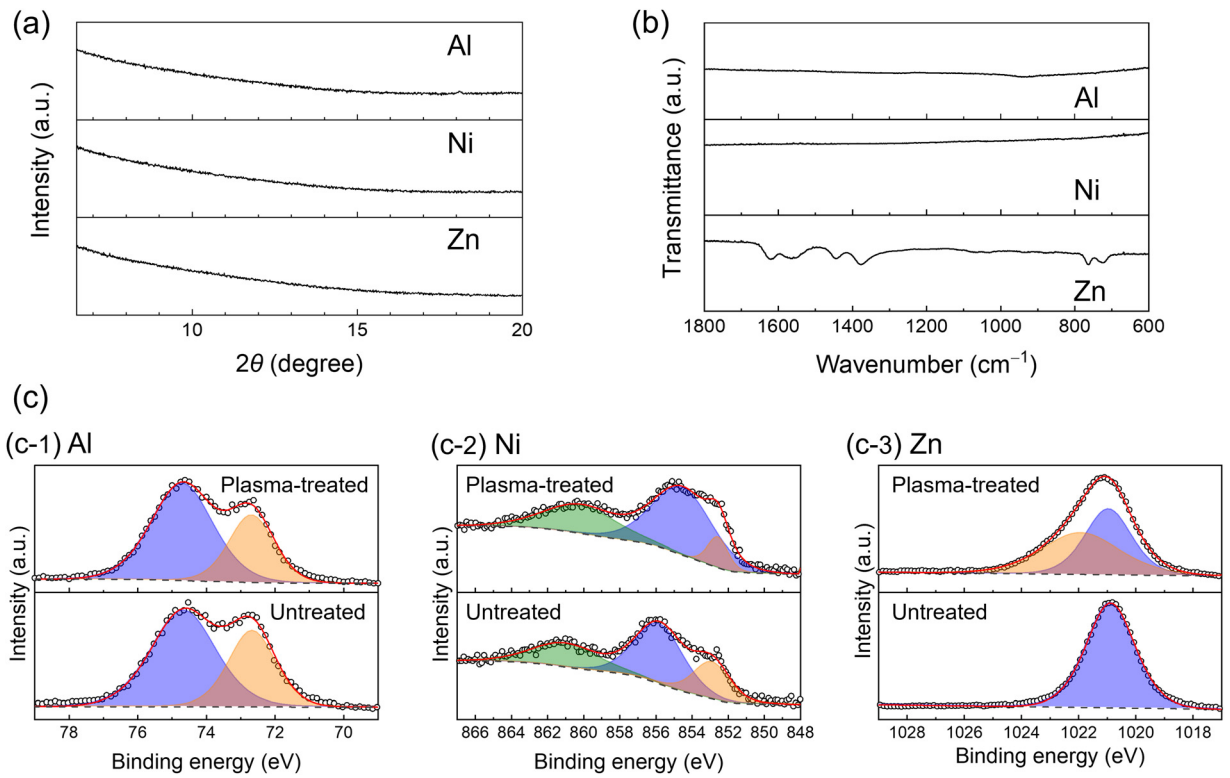

Fig. 4 Evaluation of the plasma process on different metal substrates: Zn, Ni, and Al. (a) XRD patterns and (b) FTIR spectra of plasma-treated metal substrates. (c) XPS spectra of (c-1) Al, (c-2) Ni, and (c-3) Zn. In each panel, the spectrum of the plasma-treated surface (top) is compared with that of the untreated substrate (bottom).

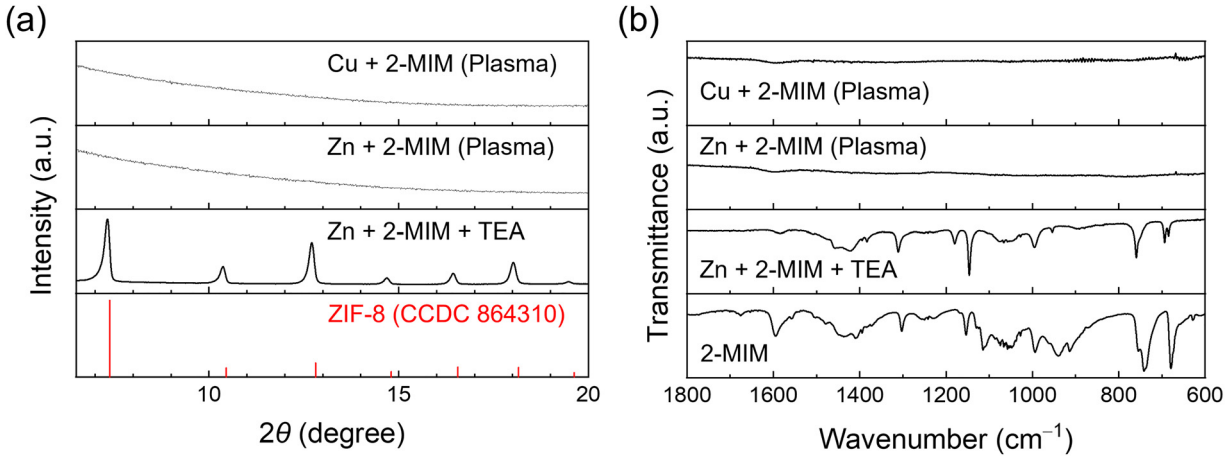

Fig. 5 Assessment of ligand specificity using 2-MIM. (a) XRD patterns and (b) FTIR spectra. The plots compare the results of plasma-treated Cu and Zn substrates (top two traces) against a chemical control sample synthesized by adding TEA to a zinc nitrate/2-MIM solution (third trace). The simulated pattern of ZIF-8 and the spectrum of the pristine 2-MIM ligand are shown at the bottom for reference.

chemical stability.[49,50] Plasma-assisted synthesis was performed on both copper and zinc substrates using a 2-MIM solution under conditions identical to those used for HKUST-1. However, as shown in the XRD patterns (Fig. 5(a)) and FTIR spectra (Fig. 5(b)), no characteristic peaks of coordination complexes were detected on either surface.

To elucidate the factors governing these results, control experiments were conducted using zinc nitrate and 2-MIM in EG. Notably, even when the mixture was subjected to solvothermal heating, which is typically sufficient for ZIF synthesis in other solvents, the solution remained clear, and no solid precipitate was formed. This indicates that in EG, thermal energy alone is insufficient to overcome the energy barrier for ligand deprotonation or displace the solvent molecules. In contrast, the addition of triethylamine (TEA) at room temperature immediately triggered the precipitation of white powders, which were confirmed to be crystalline ZIF-8 (Fig. 5(a) and (b)).

These comparative results offer valuable insights into the reaction mechanism, particularly about the role of plasma-induced reactive species in ligand deprotonation. In conventional cathodic electrodeposition, the reduction of probase molecules, such as NO^{3-}, generates OH^- ions that raise the local pH and trigger MOF crystallization by slowly deprotonating the ligands.[51] A similar chemical driving force is expected at the plasma–liquid interface. Atmospheric pressure plasma generated in contact with the precursor solution induced the formation of solvated electrons and highly reactive species, including OH^- and O_2^- from residual moisture or dissolved oxygen. Previous studies on oxygen-assisted cathodic deposition report that the generation of superoxide ions can effectively facilitate the deprotonation of organic linkers, such as H_3BTC, through the following proton-induced disproportionation reaction: $3O^{2-} + H_3BTC \rightarrow 3HO_2 + BTC^{3-}$.[52]

The plasma simultaneously drives the anodic metal dissolution from the substrate and serves as a source of reactive probes to induce deprotonation. This dual functionality represents a distinctive advantage over thermal solvothermal methods, which cannot initiate either process on a metallic substrate without additives. However, the observation that the plasma process yields an outcome consistent with the base-free conditions for 2-MIM suggests that plasma-induced basicity has inherent limitations. Although sufficient for the carboxylic acid groups of H_3BTC, where the pK_a values are in the range of 3.2 to 4.7,[53] it is unable to overcome the high energy barrier for deprotonating 2-MIM, where the pK_a is approximately 14.4. This indicates that the plasma reaction field provides a mildly basic environment, analogous to a buffer, that supports coordination only for ligands within a specific pK_a window. Consequently, plasma-assisted interfacial synthesis is constrained by synchronized kinetics and acid–base balance, highlighting its selectivity for specific metal–ligand combinations. This limitation could potentially be addressed by modulating the chemical environment of the precursor solution, as the concentration of active deprotonated linkers is governed by the solution pH relative to the ligand pK_a. Notably, the regulation of reactant speciation *via* pH control has been reported as a generalizable approach for the rapid synthesis of various MOF structures.[54] While the current base-free plasma process is restricted by the mild alkalinity generated at the plasma–liquid interface, the modulation of the initial pH or the introduction of chemical modulators may provide a pathway to overcome the deprotonation energy barriers of ligands.[54,55] Specifically, the successful anodic electrosynthesis of frameworks such as MIL-100(Fe) and MOF-5[56] suggests that these materials could be compatible with the plasma-induced anodic dissolution mechanism, provided that the solvent and atmosphere are optimized for the respective metal–ligand pairs. Furthermore, while this study focuses on the growth of continuous films, the synthesis of MOF nanoparticles might be achievable by utilizing alternative metal sources. Notably, the dispersion of metallic particles in a ligand-containing solution under plasma treatment could potentially induce nanoparticle formation, similar to the processes occurring during laser ablation in liquids.[57] Such developments would require addressing engineering challenges

related to the control of bulk nucleation and the stabilization of particles against aggregation, which represents a promising direction for broadening the utility of plasma-driven coordination chemistry.

3. Conclusion

This study demonstrates a rapid, additive-free strategy for the direct growth of MOF on metal substrates using atmospheric pressure plasma. We used HKUST-1 on a copper substrate as the model system to synthesize crystalline films within minutes in an EG solution without the need for external heating or metal precursors.

A mechanistic investigation revealed that the plasma–liquid interface functions as a unique reaction field, providing a dual driving force. Plasma treatment establishes an electrochemical circuit that triggers the anodic dissolution of metal ions from the substrate and simultaneously assists in the deprotonation of ligands by generating reactive species such as hydroxyl and superoxide ions. Specifically, the generation of superoxide ions can effectively facilitate the deprotonation of organic linkers, such as H_3BTC, through a proton-induced disproportionation reaction. This simultaneous ion supply and chemical activation are crucial for overcoming the reductive nature of organic solvents, which is insufficient to initiate conventional thermal synthesis.

Furthermore, through the expansion of the scope to different metals and ligands, interfacial film growth was found to be governed by the synchronization between the electrochemical ion supply and the acid–base kinetics. A specific processing window is defined by the standard electrode potential of the metal and the acidity of the ligand. The moderate reactivity of Cu provides a controlled ion supply that matches the crystallization kinetics, whereas the intrinsic acidity of the ligand allows deprotonation within the chemical limits of the plasma-induced environment. This strategy provides the fundamental design rules for plasma-assisted interfacial synthesis and offers a foundation for extending the process to other metal–organic systems that reside within this kinetic window.

4. Experimental section

4.1. Materials

EG, TEA, and metal nitrates, including copper(II) nitrate trihydrate, zinc nitrate hexahydrate, nickel(II) nitrate hexahydrate, and aluminum nitrate nonahydrate, were purchased from Fujifilm Wako Pure Chemical Corporation (Osaka, Japan). H_3BTC and 2-MIM were obtained from Tokyo Chemical Industry Co. Ltd (Tokyo, Japan). All the chemicals were used as received without further purification.

4.2. Plasma treatment procedures

The precursor solutions were prepared by dissolving the organic ligands (H_3BTC or 2-MIM) in EG at a concentration of 100 mM. For the synthesis, a metal foil substrate (Cu, Al, Ni, or Zn) was mounted on the ground stage of a spin coater and rotated at 1500 rpm. An aluminum rod (diameter: 4 mm) wrapped with a polyimide tape (thickness: ~60 μm) served as the high-voltage electrode. The electrode was positioned above a rotating metal substrate. Dielectric barrier discharge (DBD) was generated between the electrode and the metal substrate by applying a sinusoidal AC voltage of approximately 8–9 kV_{pp} at a frequency of 22 kHz. During the continuous plasma irradiation, 10 μL of the precursor solution was dispensed onto the center of the rotating substrate every 10 s. The centrifugal force resulting from the rotation ensured outward transport and spreading of the solution across the substrate surface. Film growth was controlled by varying the number of drop cycles. After treatment, the samples were removed, washed with ethanol to remove the unreacted species, and dried for characterization.

4.3. Solvothermal treatment of metal substrate

Metal disks (diameter: 10 mm) were immersed in 5 mL of the precursor solution (100 mM ligand in EG) in a Teflon-lined stainless-steel autoclave to investigate the reactivity of the bulk metal under thermal activation. The autoclave was sealed and heated at 150 °C for 24 h. The treated substrates were then retrieved, washed with ethanol, and dried.

4.4. Solvothermal synthesis using metal nitrates

Homogeneous solvothermal syntheses were performed using metal salts to verify the intrinsic chemical compatibility between metals and ligands. The metal nitrates (1.5 mmol) and organic ligands (1 mmol) were dissolved in EG (10 mL). The solution was transferred to a Teflon-lined stainless-steel autoclave and heated at 150 °C for 24 h. After cooling, the resulting precipitate was collected *via* filtration, washed with ethanol, and dried for further analysis.

4.5. Synthesis with triethylamine addition

To investigate the role of basicity in ligand deprotonation, a base-assisted synthesis was conducted at room temperature. The metal nitrates (1.5 mmol) and organic ligands (1 mmol) were dissolved in EG (10 mL). Subsequently, 0.2 mL of TEA was added to the solution. The mixture was then stirred at room temperature for 24 h. The obtained precipitate was filtered, washed with ethanol, and dried.

4.6. Measurements

The crystalline structure of the synthesized films and powders was analyzed by XRD using an Empyrean X-ray diffractometer (Malvern Panalytical) using Cu Kα radiation at 45 kV and 40 mA. FTIR spectra were recorded on a Shimadzu IRSpirit-X spectrometer equipped with a QATR-S single-reflection ATR accessory at a resolution of 2 cm^{-1}. The surface morphologies were observed using SEM (JEOL JSM-7800F microscope) at an accelerating voltage of 12 kV without conductive coating. The surface chemical states were investigated by XPS using a PHI5000 Versa Probe II (ULVAC PHI) with a monochromatic Al Kα source. For the plasma-treated metal foils, characterization

was performed at a radial distance of approximately 1 cm from the center of the substrate to ensure data consistency.

Author contributions

Moriyuki Kanno: conceptualization, data curation, formal analysis, funding acquisition, investigation, methodology, project administration, and writing – original draft. Tsuyohito Ito: funding acquisition, supervision, and writing – review & editing. Itaru Honma: writing – review & editing. Kazuo Terashima: funding acquisition, supervision, and writing – review & editing.

Conflicts of interest

There are no conflicts to declare.

Data availability

The data supporting this article have been included as part of the supplementary information (SI). Supplementary information: details regarding the experimental setup and electrical waveforms (Fig. S1), a comprehensive summary table of reaction outcomes across various conditions (Table S1), and additional characterization data for thermal control experiments and metal nitrate solvothermal synthesis (Fig. S2 and S3). See DOI: https://doi.org/10.1039/d6mh00065g.

Acknowledgements

The authors acknowledge the financial support from JSPS KAKENHI Grant Number 16H04506, 21H04450, and 25K17375, the ENEOS TonenGeneral Research/Development Encouragement & Scholarship Foundation, and the Iketani Science and Technology Foundation.

Notes and references

1 D. Li, A. Yadav, H. Zhou, K. Roy, P. Thanasekaran and C. Lee, *Global Challenges*, 2024, **8**, 2300244.
2 W. Wang, D. Chen, F. Li, X. Xiao and Q. Xu, *Chem*, 2024, **10**, 86–133.
3 H.-C. Joe Zhou and S. Kitagawa, *Chem. Soc. Rev.*, 2014, **43**, 5415–5418.
4 Q. Zhang, S. Yan, X. Yan and Y. Lv, *Sci. Total Environ.*, 2023, **902**, 165944.
5 K. Takagi, M. Kanno, H. Muneoka, K. Terashima and T. Ito, *Appl. Phys. Lett.*, 2024, **124**, 124101.
6 D. L. Zhao, F. Feng, L. Shen, Z. Huang, Q. Zhao, H. Lin and T.-S. Chung, *Chem. Eng. J.*, 2023, **454**, 140447.
7 A. Zuliani, N. Khiar and C. Carrillo-Carrión, *Anal. Bioanal. Chem.*, 2023, **415**, 2005–2023.
8 X. Shi, Y. Shan, M. Du and H. Pang, *Coord. Chem. Rev.*, 2021, **444**, 214060.
9 P. Su, M. Tu, R. Ameloot and W. Li, *Acc. Chem. Res.*, 2022, **55**, 186–196.
10 A. Knebel and J. Caro, *Nat. Nanotechnol.*, 2022, **17**, 911–923.
11 A. A. Bhoite, K. V. Patil, R. S. Redekar, P. S. Patil, V. A. Sawant and N. L. Tarwal, *J. Solid State Chem.*, 2023, **326**, 124192.
12 W. Li, Y. Zhang, Z. Yu, T. Zhu, J. Kang, K. Liu, Z. Li and S. C. Tan, *ACS Nano*, 2022, **16**, 14779–14791.
13 D.-H. Chen, H. Gliemann and C. Wöll, *Chem. Phys. Rev.*, 2023, **4**, 011305.
14 Y. Lin, W.-H. Li, Y. Wen, G.-E. Wang, X.-L. Ye and G. Xu, *Angew. Chem., Int. Ed.*, 2021, **60**, 25758–25761.
15 S. Goswami, M. Rimoldi, R. Anderson, C. Lee, X. Li, A. Li, P. Deria, L. X. Chen, R. D. Schaller, D. A. Gómez-Gualdrón, O. K. Farha and J. T. Hupp, *Chem. Mater.*, 2022, **34**, 9446–9454.
16 R. Xu, Y. Kang, W. Zhang, X. Zhang and B. Pan, *Angew. Chem., Int. Ed.*, 2022, **61**, e202115443.
17 X.-J. Bai, X.-Y. Lu, R. Ju, H. Chen, L. Shao, X. Zhai, Y.-N. Li, F.-Q. Fan, Y. Fu and W. Qi, *Angew. Chem., Int. Ed.*, 2021, **60**, 701–705.
18 J. B. Decoste, G. W. Peterson, M. W. Smith, C. A. Stone and C. R. Willis, *J. Am. Chem. Soc.*, 2012, **134**, 1486–1489.
19 Z. Jiang, L. Ge, L. Zhuang, M. Li, Z. Wang and Z. Zhu, *ACS Appl. Mater. Interfaces*, 2019, **11**, 44300–44307.
20 Q. Qi, D. Shao, Y. Zhou, Q. Wang and X.-Y. Yu, *J. Mater. Chem. A*, 2023, **11**, 15663–15669.
21 X. Kong, G. Liu, H.-Q. Peng, Z. Xu, S. Bu, B. Liu and W. Zhang, *J. Mater. Chem. A*, 2022, **10**, 6596–6606.
22 A. Moghaddasfar, G. M. Ziarani, R. Luque and A. Badiei, *Mater. Adv.*, 2025, **6**, 3416–3432.
23 M. Kanno, T. Ito and K. Terashima, *Plasma Processes Polym.*, 2024, **21**, 2300156.
24 M. Kanno, T. Ito, Y. Shimizu and K. Terashima, *Plasma Processes Polym.*, 2021, **18**, 2100047.
25 S. Chiba, M. Kanno, H. Muneoka, T. Ito and K. Terashima, *Jpn. J. Appl. Phys.*, 2024, **63**, 036001.
26 M. Kanno, T. Kitao, T. Ito and K. Terashima, *RSC Adv.*, 2021, **11**, 22756–22760.
27 Z. Karimzadeh, B. Shokri and A. Morsali, *Sci. Rep.*, 2023, **13**, 15156.
28 Q. Wei, S. Xue, W. Wu, S. Liu, S. Li, C. Zhang and S. Jiang, *Chem. Rec.*, 2023, **23**, e202200263.
29 A. M. Lister, B. I. Armitage, Y. Wang, R. Chen, W. Li and M. R. Castell, *ACS Appl. Nano Mater.*, 2025, **8**, 15114–15121.
30 Y. Liu, Y. Wei, M. Liu, Y. Bai, X. Wang, S. Shang, J. Chen and Y. Liu, *Angew. Chem., Int. Ed.*, 2021, **60**, 2887–2891.
31 W. Guo, W. Zhang, N. Han, S. Xie, Z. Zhou, W. Monnens, O. Martinez Mora, Z. Xue, X. Zhang, X. Zhang and J. Fransaer, *Chem. – Eur. J.*, 2023, **29**, e202302338.
32 S. S. A. Al-Qaisi, A. Raisi and Q. F. Alsalhy, *Sci. Rep.*, 2025, **15**, 14636.
33 P. Sharma, A. Jatrana, S. Mondal, S. Maan and V. Kumar, *ChemistrySelect*, 2023, **8**, e202204312.
34 M. Mohammadnejad, A. Roshan and S. Geranmayeh, *Cellulose*, 2024, **31**, 535–550.
35 N. H. N. Azman, M. M. Alias and Y. Sulaiman, *Energies*, 2023, **16**, 7072.

36 S. Poulston, P. M. Parlett, P. Stone and M. Bowker, *Surf. Interface Anal.*, 1996, **24**, 811–820.
37 K. Okada, R. Ricco, Y. Tokudome, M. J. Styles, A. J. Hill, M. Takahashi and P. Falcaro, *Adv. Funct. Mater.*, 2014, **24**, 1969–1977.
38 K. Okada, S. Sawai, K. Ikigaki, Y. Tokudome, P. Falcaro and M. Takahashi, *CrystEngComm*, 2017, **19**, 4194–4200.
39 J. Zhao, W. T. Nunn, P. C. Lemaire, Y. Lin, M. D. Dickey, C. J. Oldham, H. J. Walls, G. W. Peterson, M. D. Losego and G. N. Parsons, *J. Am. Chem. Soc.*, 2015, **137**, 13756–13759.
40 K. Ikigaki, K. Okada, Y. Tokudome and M. Takahashi, *J. Sol-Gel Sci. Technol.*, 2019, **89**, 128–134.
41 K. Okada, K. Mori, A. Fukatsu and M. Takahashi, *J. Mater. Chem. A*, 2021, **9**, 19613–19618.
42 G. Majano and J. Pérez-Ramírez, *Adv. Mater.*, 2013, **25**, 1052–1057.
43 H. Yue, Y. Zhao, X. Ma and J. Gong, *Chem. Soc. Rev.*, 2012, **41**, 4218–4244.
44 Y. Wang, Y. Chen, Y. Zhou, Y. Wang, Y. Wu, Y. Xie, P. Zhao, X. Hu and J. Fei, *Microchim. Acta*, 2024, **191**, 393.
45 D. Mohanadas, M. A. A. Mohd Abdah, N. H. N. Azman, T. B. S. A. Ravoof and Y. Sulaiman, *Sci. Rep.*, 2021, **11**, 11747.
46 F. L. Hutson, D. E. Ramaker and B. E. Koel, *Surf. Sci.*, 1991, **248**, 104–118.
47 G. Greczynski, D. Primetzhofer and L. Hultman, *Appl. Surf. Sci.*, 2018, **436**, 102–110.
48 Y.-X. Dai, W.-L. Xin, L.-H. Xu, J. Li, Y.-X. Li, J. Li, S. Cosnier, X.-J. Zhang, R. S. Marks and D. Shan, *Appl. Surf. Sci.*, 2022, **591**, 153066.
49 Z. Lai, *Curr. Opin. Chem. Eng.*, 2018, **20**, 78–85.
50 A. Paul, I. K. Banga, S. Muthukumar and S. Prasad, *ACS Omega*, 2022, **7**, 26993–27003.
51 M. Li and M. Dincă, *Chem. Sci.*, 2013, **5**, 107–111.
52 Y. Xiao, Z. Wu, Q. Zhang, P. Li, H. Yu and G. Lu, *Cryst. Growth Des.*, 2020, **20**, 3997–4004.
53 Y. Ma, K. C. Gross, C. A. Hollingsworth, P. G. Seybold and J. S. Murray, *J. Mol. Model.*, 2004, **10**, 235–239.
54 L. Huelsenbeck, H. Luo, P. Verma, J. Dane, R. Ho, E. Beyer, H. Hall, G. M. Geise and G. Giri, *Cryst. Growth Des.*, 2020, **20**, 6787–6795.
55 Y. Liu, H. Chen, T. Li, Y. Ren, H. Wang, Z. Song, J. Li, Q. Zhao, J. Li and L. Li, *Angew. Chem.*, 2023, **135**, e202309095.
56 H. Al-Kutubi, J. Gascon, E. J. R. Sudhölter and L. Rassaei, *ChemElectroChem*, 2015, **2**, 462–474.
57 N. Motakef-Kazemi, F. Ataei and D. Dorranian, *Opt. Quant. Electron.*, 2023, **55**, 921.